

Heating rates in a thin ion trap for microcavity experiments

E. Brama · A. Mortensen · M. Keller · W. Lange

Received: 11 August 2011 / Revised version: 22 December 2011
© Springer-Verlag 2012

Abstract We have built and characterized a novel linear ion trap. Its small horizontal electrode separation of 250 μm would previously have required microfabrication methods, while our trap was machined conventionally. The thin trap is designed to accommodate a transverse optical cavity of 0.5 mm length, a requirement for cavity-QED experiments with trapped ions in the strong coupling regime. The sandwich structure of the electrodes allows for a very accurate alignment. Employing the Doppler-recooling method, we found that intermittent laser-induced radiation pressure has a significant effect on the ion's spectrum. This must be taken into account to correctly determine the heating rate of the trap. To this end, we have derived an analytic expression for the spectral line shape of the ion, which includes the effect of natural line broadening, heating as well as radiation pressure. We apply it to determine the accurate heating rate of the system.

1 Introduction

Radio-frequency ion-traps have become an important tool in a wide range of applications in atomic physics, quantum information science, quantum optics, and even chemistry. Trapped ions have been used to test precisely our understanding of the interaction of light and matter [1], to achieve the highest accuracy in atomic spectroscopy [2, 3], to implement high-fidelity quantum gates [4, 5], and to generate multi-ion entanglement [6]. The excellent localization of laser-cooled ions in the trapping potential [7] makes them

a promising system for deterministic single-photon sources [8, 9] and atom-light interfaces with applications in entanglement distribution and as nodes of quantum networks [10].

In recent years, electrode structures with diverse designs have been implemented to provide a ponderomotive trapping potential, with trap sizes ranging from several cm to tens of μm . While early ion traps had cylindrically symmetric parabolic electrodes matching the equipotential surfaces of the quadrupole field of an ideal Paul trap, most modern rf traps have linear geometry to store strings of ions. An approximate quadrupole field in the radial direction is generated by four linear electrodes, for example, cylindrical rods or metal blades. With increasing miniaturization, trap construction has moved from manual assembly of conventionally machined parts to employing microfabrication methods used in semiconductor manufacturing [11]. Recently, surface traps with planar electrodes have been developed, significantly simplifying the process of microfabrication [12]. Even though monolithic ion traps offer very accurate alignment and potentially very low heating rates [13], the majority of nonplanar traps are still based on manually assembled structures which are manufactured using laser or conventional machining. The advantages are comparatively low cost and fast turn-around times.

In this paper, we present an ion-trap design which is particularly well suited for cavity-QED experiments in which the trap is combined with an optical cavity of small mode volume. It is built from conventionally machined components which are assembled to form a miniature linear ion trap with an ion-electrode distance of 166 μm . It provides large secular frequencies and high alignment accuracy through self-aligning elements. We have built a prototype of the trap and tested its operation thoroughly.

In the first part of the paper, we describe the trap geometry and assembly of the trap elements. We proceed

E. Brama · A. Mortensen · M. Keller (✉) · W. Lange
Department of Physics and Astronomy, University of Sussex,
Brighton, BN1 9QH, UK
e-mail: m.k.keller@sussex.ac.uk

by presenting characteristic trap parameters we have measured, and finally report the results of heating rate measurements based on the analysis of fluorescence at the onset of Doppler-recooling. We show the importance of laser induced radiation pressure in these measurements and derive an analytic expression for the spectral line-shape of an ion exposed to heating following a change in radiation pressure. We use this result in conjunction with an extrapolation method that allows us to evaluate the ion's fluorescence at the onset of recooling, independent of a model for the recooling dynamics. With this new method, we can reliably determine the ion's temperature after a controlled heating phase. In spite of the limited quality of the electrode surfaces and the unusual choice of the electrode material, the heating rate measured in this way is comparable to that found in traps of similar size.

2 Trap geometry and assembly

Construction of the trap presented here was motivated by its application for cavity-QED with small ion strings under strong coupling conditions. Strong coupling of the ions to the optical field in the cavity requires a small mode volume and hence a small distance between the cavity mirrors on the order of a few $100\ \mu\text{m}$. We had previously found [14] that placing dielectric mirrors inside the rf field used for the radial confinement of ions leads to distortions of the field, deteriorating trapping conditions. In order to reduce the overlap between electric rf field and cavity mirrors, a small trap with a well-confined rf field is required, which fits between two closely spaced mirrors. This is the reason for designing a trapping structure with thin electrodes, suitable for strongly coupled cavity-QED experiments with trapped ions.

In order to reduce the coupling between axial and radial components of the ions' motion, the electrodes need to be precisely aligned. The presence of an axial component of the rf field would deteriorate localization of the ions in an optical cavity. Our design is based on a linear ion trap as described in Ref. [7]. Perpendicular to the trap axis, the ions are confined by an rf potential generated by four electrodes. The desired small thickness of the trap is achieved by using thin metal sheets. They are made from highly conductive oxygen free (HCOF) copper with a thickness of $125\ \mu\text{m}$. To confine the ions along the trap axis, dc electrodes at positive potential are located between the rf electrodes [see Figs. 1 and 2(b)]. They, too, are made from an HCOF copper sheet with a thickness of $100\ \mu\text{m}$ and have a width of $1\ \text{mm}$. The dc electrodes are insulated from the rf electrodes by a $75\ \mu\text{m}$ thick Kapton foil. In order to avoid dielectric material in the close vicinity of the ions, the Kapton foil is recessed by $1\ \text{mm}$ from the trapping region. There are 8 dc electrodes

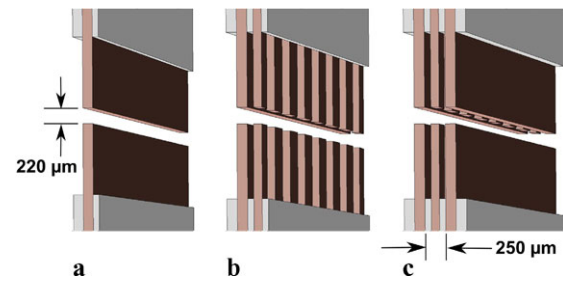


Fig. 1 Drawings of the trap electrodes (brown) and the Kapton foil (gray) incrementally showing the different electrode layers. Figure (a) shows the two rf electrodes in the rear layer. The vertical spacing between the electrodes is $220\ \mu\text{m}$. The copper foil strips used for axial ion confinement are added in (b). In between each pair of neighboring electrode strips is a separate ion trapping zone. In (c) the two front rf electrodes have been added to show the full electrode structure

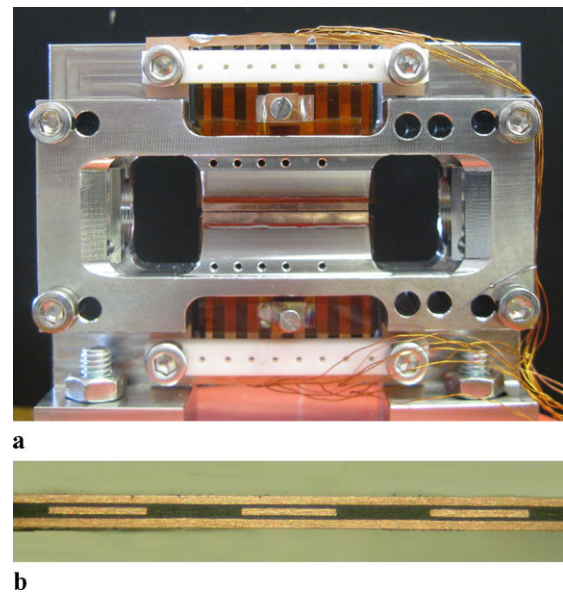


Fig. 2 (a) Photograph of the trap assembly from the side, showing the narrow slit between the upper and lower electrodes. At the top and at the bottom, the electrical connectors are visible. (b) Top view of the lower electrode assembly, showing three dc electrodes in the central layer, sandwiched between the two rf electrodes

along the trap axis with a separation of $1.5\ \text{mm}$, forming 7 trapping zones between adjacent electrode pairs. The total distance between the rf electrodes is $250\ \mu\text{m}$ and the entire stack of electrodes is $500\ \mu\text{m}$ thick, so that it can be fitted inside an optical cavity of $500\ \mu\text{m}$ length. Sandwiching the different layers leads to a high mechanical stability of the structure.

Even though the numerical simulations have shown that the trap design is robust against misalignment of the electrodes, great care has been taken to optimize alignment of the dc electrodes. Instead of inserting the dc electrodes separately in between the rf electrodes, the set of 8 electrodes has been machined out of one copper sheet with all electrodes still connected in a comb structure. The upper and lower

half of the trap are assembled by stacking the three electrode and separating Kapton layers as shown in Fig. 1 and aligning the electrodes by carefully pushing them against a mechanical stop. The two electrode assemblies are then mounted opposite each other, forming an rf trap with a vertical electrode separation of 220 μm . This is assured by temporarily inserting a mechanical spacer. The trap assembly is then fixed with a Kapton insulated metal clamp as shown in Fig. 2. Care is taken to avoid deformation of the electrodes when removing the spacer. Alignment is controlled using a microscope. In the clamped trap, the dc electrodes are separated by removing the connecting bridge. With the design of the trap electrodes and the alignment procedure, the separation of upper and lower part of the trap is constant to better than 10 μm over the entire length of the trap (20 mm). The transverse spacing of the electrode layers is constant to within 3 μm . The machining of the thin metal foils for the trap construction must not exert large forces on the foil in order to avoid deformation of the electrodes. For this reason, we have employed wire eroding. However, the surface quality of the machined parts with a roughness of about 10 μm rms is worse than for standard milling and may lead to an increased heating rate [15].

We have characterized the performance of the trap by numerically calculating the trapping potentials with a finite element code (FEMLAB). The pseudopotential, which determines the motion of the ion in the plane perpendicular to the trap axis, is shown in Fig. 3 for typical experimental parameters. The radial secular frequency of the ion-trap can be expressed as

$$\omega_r = \eta \frac{\sqrt{2} Q V_{\text{ac}}}{m \Omega r_0^2}. \quad (1)$$

Here, Q and m are the charge and mass of the ion, V_{ac} is the amplitude of the potential applied to the rf electrodes, Ω is the rf frequency, and r_0 is the shortest distance between the ion and the electrode (166 μm in our case). In order to quantify the deviation of the radial trapping potential from an ideal quadrupole potential, the trap efficiency η is employed, specifying the ratio of the actual secular frequency and the secular frequency in a corresponding ideal quadrupole trap with symmetric parabolic electrodes. The numerically obtained trap efficiency for our geometry is $\eta = 0.75$.

The anharmonicity of the ponderomotive potential can be characterized by decomposing the potential in a Taylor expansion and comparing the amplitudes with the harmonic term. These ratios perpendicular to the electrode plane (horizontal) and parallel to the electrode plane (vertical) are summarized in Table 1. Similarly, we have analyzed the axial confinement and compared it with an ideal harmonic potential. From the harmonic term of the Taylor expansion, the confinement strength can be derived to be $\nu_z = 120 \text{ kHz} \sqrt{V_{\text{dc}}}$, which is in agreement with our measurement.

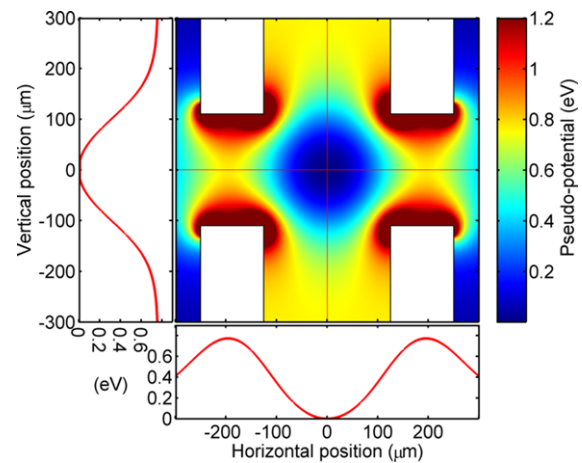


Fig. 3 Radial cross-section of the pseudo-potential of the linear trap at the trap center for $V_{\text{ac}} = 20 \text{ V}$, obtained from a finite element calculation by averaging the potential over one rf cycle. Profiles of the pseudo-potential in the vertical and horizontal direction are shown at the edge of the two-dimensional plot

Table 1 Relative size of anharmonic contributions to the radial ponderomotive (rf) and axial (dc) confinement. C_n is the coefficient in the Taylor expansion of the pseudopotential or potential. The anharmonicity in each direction was evaluated at a distance $l_0 = 10 \mu\text{m}$, corresponding to the scale of a two-ion crystal in the axial direction for our experimental parameters

Anharmon. coefficient	Horiz. rf confinem.	Vert. rf confinem.	Axial dc confinem.
$C_4 l_0^2 / C_2$	7×10^{-4}	6×10^{-4}	9×10^{-4}
$C_6 l_0^4 / C_2$	8×10^{-6}	-7×10^{-6}	3×10^{-7}
$C_8 l_0^6 / C_2$	-8×10^{-9}	-2×10^{-8}	1×10^{-10}

An important issue for use of the trap in conjunction with a transverse optical cavity is the influence of the dielectric mirrors on the trapping potential. We have numerically determined the pseudo-potential in the presence of mirrors with dielectric constant $\epsilon_r = 3.75$ at the minimum separation of 500 μm . The resulting change in the radial frequency was 0.5 % compared to the case without mirrors. This confirms that the trap meets the design criterion of resilience against dielectric materials in close proximity to the trap.

3 Experimental set-up and trap characteristics

The ion trap assembly is installed in a small vacuum chamber. Large windows sealed with indium wire provide good optical access from four sides. The rf generator resonantly drives an LC circuit containing the trap rf electrodes, supplying them with an amplitude of up to 100 V at a frequency of $\Omega = 2\pi \times 22.68 \text{ MHz}$. The rf voltage is applied to two diagonally opposed rf electrodes with the other two electrodes kept at rf ground. Dc voltages for confinement of the

ions along the trap axis are controlled by computer using a D/A card. In order to suppress rf pick-up, the dc electrodes are grounded through capacitors which are soldered directly to the electrodes. An important issue in ion traps are radial stray electric fields, which push the ions off the rf field minimum, making them undergo a driven motion at the rf frequency (micromotion). To avoid this, any dc fields perpendicular to the trap axis are carefully compensated by adding dc voltages to the rf electrodes through RC circuits. Each of the four dc offsets is controlled individually through the D/A card.

In our experiments, we trap and laser-cool $^{40}\text{Ca}^+$ ions. The trap is loaded with $^{40}\text{Ca}^+$ ions by photo-ionization of neutral calcium. The laser beams for photo-ionization intersect an effusive beam of neutral calcium atoms emanating from a 10 mm long tantalum tube containing solid calcium. The tube is resistively heated to a few hundred degree Celsius by sending a current of 1.5 A through two tantalum wires spot-welded to each end of the tube. The ionization of neutral calcium is performed first by resonantly exciting neutral calcium from the $4s^2 \ ^1S_0$ ground state to the $4s4p \ ^1P_1$ excited state using a laser at 422 nm and then ionizing the atom from this state using 389 nm laser light [16].

The ions are Doppler-cooled on the $4S_{1/2}$ to $4P_{1/2}$ transition with two 397 nm laser beams. Each beam has an optical power of about 5 μW and is focused down to a waist of 25 μm radius at the ion position. The two 397 nm laser beams are propagating almost in the horizontal plane, at angles of $\pm 20^\circ$ with respect to the trap axis and 140° with respect to each other. To ensure that all principal axes of the trap are cooled and that micro-motion in both the horizontal and vertical direction can be probed and minimized [17], one of the beams has an inclination of about 4° with respect to the horizontal plane.

In addition to the 397 nm cooling laser, two infrared lasers at 850 nm and 854 nm are used in the laser cooling cycle. They are required for pumping the ion out of the metastable $3D_{3/2}$ -state populated by spontaneous decay from the $4P_{1/2}$ -state excited during laser cooling. The 850 nm laser is resonant with the transition from the $3D_{3/2}$ to the $4P_{3/2}$ -state, from which the ion can decay to the ground state again. There is an additional decay channel from $4P_{3/2}$ to the $3D_{5/2}$ -state, from which the ion is repumped with the laser at 854 nm. Repumping via the $4P_{3/2}$ -state rather than $4P_{1/2}$ eliminates coherent population trapping to the $3D_{3/2}$ -state and thus reduces the level scheme of the calcium-ion to an effective two-level system.

The 397 nm light for laser-cooling is generated by a commercial frequency doubled laser system. It is stabilized against frequency drifts using a scanning cavity lock which is described in detail elsewhere [18]. For absolute optical frequency reference, the scanning cavity lock utilizes a diode laser system at 894.6 nm, locked to a tunable cavity with a Pound–Drever–Hall scheme, which in

turn is stabilized to the cesium D_1 line using polarization spectroscopy. The scanning cavity laser lock provides an overall absolute stability of better than 100 kHz at 397 nm. The 850 nm and the 854 nm repumping lasers are extended cavity diode lasers. They are frequency stabilized through slow feedback from a computer controlled wavelength-meter (High Finesse WS-7). All laser light is delivered to the vacuum chamber through single-mode polarization-maintaining optical fibers. The amount of optical power in each of the two 397 nm cooling laser beams and the 854 nm repumping beam are controlled using the first-order diffracted beam in a double pass acousto-optic modulator before entering the optical fiber. The laser beams are finally focused to a waist of 25 μm at the ion position using lenses placed outside the vacuum chamber.

We have probed the confining potential of the ion trap by applying a small modulation voltage to one of the rf electrodes or one dc electrode. Observing a dip in the fluorescence of the ions while scanning the modulation frequency indicates a motional resonance of the trap. Using this method for different amplitudes V_{ac} of the rf voltage, we find that stable trapping is obtained for radial secular frequencies in the range of $\nu_r = 0.8\text{--}5$ MHz. For weaker radial confinement, the trapping time as well as loading efficiency is decreased. In the experiments presented here, a radial secular frequency of $\nu_r = 1.5$ MHz was chosen, corresponding to an rf-drive amplitude $V_{\text{ac}} = 14.5$ V. Axial confinement of the ion between two adjacent electrode strips [see Fig. 1(b)] is obtained by applying a positive bias potential of $V_{\text{dc}} = 20$ V to the strips, resulting in an axial trapping frequency $\nu_z = 575$ kHz.

As mentioned above, the presence of stray electric fields can displace the ion from the nodal line of the rf trapping fields along the trap axis. The ion then undergoes driven radial oscillations at the trap frequency Ω , which leads to line broadening, heating, and reduced coupling to the field, for example in an optical cavity. To compensate the stray fields and hence avoid micro-motion, we apply additional dc offset voltages to the rf electrodes. To determine the compensation voltages required, the ion's fluorescence is measured in correlation with the rf-drive of the trap. If micro-motion is present, the correlation signal is modulated at the drive frequency due to the Doppler effect. By using two non-collinear lasers, we find the compensation voltages to eliminate micromotion in both radial directions. The residual modulation of fluorescence for an ion after compensation of micromotion is less than 1 % of the total fluorescence level detected. This corresponds to a residual motional amplitude of the ion of below 8 nm which is two orders of magnitude lower than the size of the standing wave structure of the cavity mode. This is essential for achieving deterministic ion-cavity coupling.

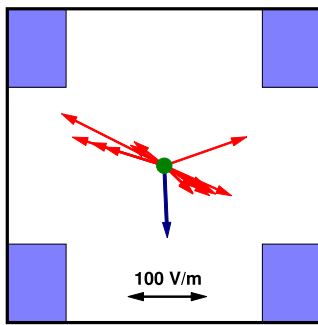


Fig. 4 Average direction of stray fields (*blue arrow*) as well as deviations (*red arrows*), obtained by subtracting the average from each individual stray field measurement. The position of the rf electrodes in the four corners is indicated. Data were taken over a period of 129 days. The direction of the day-to-day deviations during this time appears mainly along one diagonal. The scale of the deviations in V/m is indicated at the bottom

The compensation voltages, and hence the stray fields obtained in this way changed during the period of data acquisition. Over 129 days, the compensation electric fields varied between -88 V/m and 106 V/m in the horizontal direction and -135 V/m and -47 V/m in the vertical. The average shift observed during this time was in the vertical direction. The size of variations around this average was statistical. In Fig. 4, the average stray field is shown along with the daily deviations. It is striking that the variations occur predominantly along one diagonal between two rf electrodes, indicating that stray fields originate on one or two diagonally opposite electrodes. This is in keeping with the fact that the ion trap is loaded in situ, leading to an asymmetric coating of the rf electrodes with calcium during the loading procedure. This is expected to result in patch potentials which change during the loading of the ion trap [19].

4 Spectrum of ion with intermittent cooling

An important issue related to fluctuating patch potentials on the trap electrodes and the small ion-electrode distance is heating of the ions' motion. It has a direct impact on the localization of the ions and the minimum vibrational excitation that can be achieved by laser cooling. The heating rate scales inversely to the fourth power of the ion-electrode distance [20, 21]. In a miniature trap like the one presented here, heating is therefore expected to be strong and it is important to ascertain that heating is manageable. In experiments where low thermal excitation is achieved by using resolved sideband cooling, a precise measurement of heating rates from the strength of the sidebands is possible [20–22]. We have employed a simpler method to measure the heating rate of the trap, based on the one demonstrated by Epstein et al. [23]. By suspending Doppler-cooling for a given time, the ions experience a period of exclusive heating, increasing

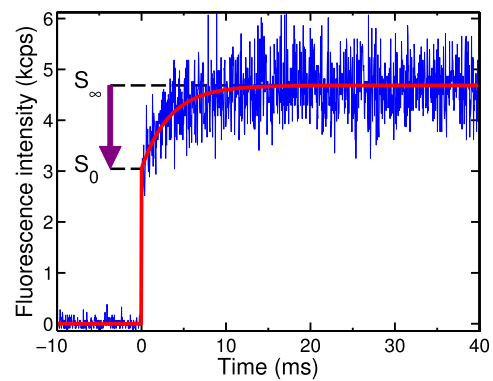


Fig. 5 Ion fluorescence as a function of time, with the recooling laser switched on at $t = 0$. The red curve is an exponential fit to the function $S(t) = S_\infty + (S_0 - S_\infty) \cdot \exp(-t/\tau)$. Fit parameters: $\tau = 3.4$ ms, $S_0/S_\infty = 0.66$

their thermal motion in proportion to the heating rate. After switching the cooling laser back on, the time-resolved fluorescence of the ions during Doppler-recooling can be employed to obtain the temperature at the end of the heating phase. The fluorescence level of the ion changes since the ion's spectrum is narrowed as the ion is cooled. For small detunings, fluorescence increases with decreasing temperature, while for large detunings, fluorescence decreases. A typical fluorescence curve in our experiment is shown in Fig. 5, with the recooling laser switched on at $t = 0$. As can be seen from the figure, the ion's fluorescence, starting from S_0 at $t = 0$, approaches the equilibrium value S_∞ on a time-scale of $\tau = 3.4$ ms.

In the setup commonly used for the Doppler-recooling method, heating of the ion's motion is not the only effect of switching off the Doppler-cooling laser. In order to provide axial cooling, this laser must have a component in the direction of the trap axis. In our set-up, it subtends an angle of 20° with the axis. Consequently, the cooling laser exerts radiation pressure on the ion along the axis. While the cooling laser is on, radiation pressure displaces the equilibrium position of the ion away from the center of the axial potential well. When the cooling is suddenly switched off at the beginning of the heating period, the ion is left in a displaced position in the potential well and starts to oscillate along the trap axis, with an amplitude equal to the initial displacement z_0 . In the experiment, this displacement cannot be observed directly, but the corresponding oscillation has a significant influence on the spectrum of the ion. It leads to a Doppler shift peaking at a value of Δ_0 , which is related to the oscillation amplitude z_0 by

$$\Delta_0 = 2\pi \frac{z_0}{\lambda} \omega_z, \quad (2)$$

where λ is the wavelength of the radiation and $\omega_z = 2\pi \times \nu_z$ is the oscillation frequency of the ion along the trap axis.

Intermittent radiation pressure in the *radial* direction leads to a much smaller displacement, due to the much

stronger radial confinement. However, even a small radial displacement, moving the ion away from the node of the trapping field, results in increased micromotion, as discussed in Sect. 3. Both micromotion and axial oscillations contribute to the observed Doppler shift in the spectrum and must be taken into account when determining the ion's temperature. Ignoring these effects may lead to a considerable overestimation of the ion's temperature by falsely attributing a thermal origin to the oscillatory motion. To our knowledge, the effect of radiation pressure has not been considered in previous heating rate measurements based on the method introduced in Ref. [23], even though it can be significant.

To distinguish unambiguously between thermal motion and radiation-pressure induced oscillations, information on the ion's fluorescence *spectrum* is required. In the Appendix, we derive an expression for the spectrum of the ion taking into account power broadening, described by a homogeneous linewidth γ , thermal broadening described by an inhomogeneous linewidth σ and oscillatory broadening described by the associated maximum Doppler shift Δ_0 from Eq. (2). For an ion at temperature T , Doppler-broadening leads to

$$\sigma = \frac{2\pi}{\lambda} \sqrt{\frac{k_B T}{m}}. \quad (3)$$

Solving for the temperature, we obtain

$$T = \frac{m\lambda^2\sigma^2}{4\pi^2 k_B}. \quad (4)$$

For calcium ions, this expression evaluates to $T[\text{mK}] = 0.758 (\sigma[\text{MHz}])^2$. As shown in the Appendix, the resulting spectrum is given by the analytic function

$$S_{\text{heated}}(\delta, \gamma, \sigma, \Delta_0) = \text{Re} \left[\frac{w(\sqrt{z-d}) - i w(\sqrt{d-z^*}) + i e^{-d} w(\sqrt{-z^*})}{\sqrt{2\pi}\sigma(2 - e^{-d})} \right] \quad (5)$$

where δ is the detuning of the cooling laser from resonance,

$$z = \frac{(|\delta| + i\gamma)^2}{2\sigma^2}, \quad d = \frac{\Delta_0^2}{2\sigma^2}$$

and $w(z)$ is the complex error function defined in Eq. (15) in the Appendix.

For short heating periods, which is the case relevant here, we have $\sigma < \Delta_0$. The spectrum is then best described as oscillatory with an amplitude distribution broadened by thermal effects. It is clearly different from the Voigt profile one would expect in thermal equilibrium. An example is given in Fig. 6. The blue curve is the power-broadened Lorentzian spectrum of a laser-cooled ion, corresponding to $S_{\text{cooled}} = S_{\infty}(\delta)$. The red curve represents the spectrum a certain time after switching off the cooling laser, according

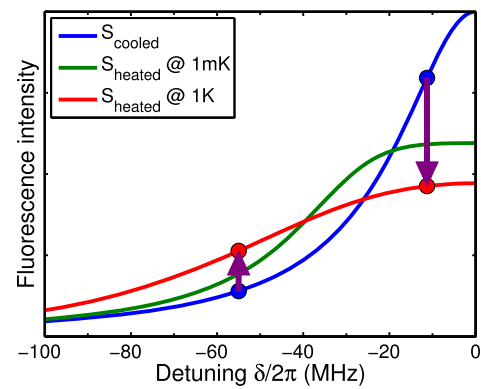


Fig. 6 Calculated spectra S_{cooled} for a cooled ion (*blue*) and S_{heated} for a heated ion at a temperature of 1 K (*red*). Expressions for the spectra are derived in the Appendix. The arrows show the difference in fluorescence level between the two cases. Only part of the effect is due to thermal motion. Another contribution is due to an harmonic oscillation, triggered by switching off the cooling laser. This results in the intermediate spectrum (*green*), which displays significant line broadening, even for a cold ion at 1 mK

to Eq. (5). It takes into account thermal effects and oscillatory motion. As expected, the direction of change in fluorescence level depends on detuning. Close to resonance, the fluorescence level drops as a result of switching off the cooling laser, while for large detuning it increases. In Fig. 6, the change in fluorescence level from cooled to heated ion is indicated at two selected detunings.

To illustrate how much of the spectral redistribution is due to the ion's oscillation, we show in the same graph a spectrum with negligible thermal broadening but otherwise identical parameters (*green* fluorescence trace). At the two indicated detunings, roughly half the effect is due to the harmonic oscillation of the ion. By fitting the spectrum of the ion following a period of suspended cooling using Eq. (5), we can determine the homogeneous linewidth of the ion, its oscillation amplitude and, most importantly, the correct inhomogeneous linewidth. From the latter, the temperature follows directly according to Eq. (4).

5 Heating rates

The approach we follow to measure the temperature of the ion is more general than that of Wesenberg et al. [24], as it does not require any assumptions about details of the re-cooling process other than that the fluorescence level rises or falls linearly at the onset of re-cooling. This is well confirmed by our experimental data during the first 600 μs (see Fig. 7).

The most important quantity to determine is the fluorescence level at the moment the cooling laser is switched on ($t = 0$). In practice, it depends on the size of the time-bins chosen to evaluate detector counts. A larger bin-size

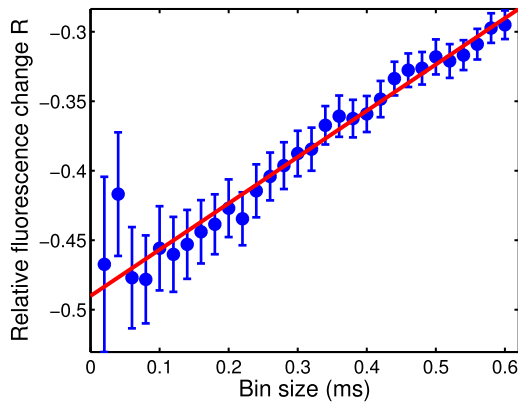


Fig. 7 Relative change $R = (S_0/S_\infty - 1)$ of fluorescence in the first bin after recoiling starts, as a function of bin-size. The linear increase is evident and allows us to extrapolate the results to zero bin-size, giving us an accurate value for the relative fluorescence level at $t = 0$

decreases fluctuations of the counting statistics but introduces a systematic error caused by the influence of recoiling during the sampling period, which changes the fluorescence level. Immediately following the switch-on of recoiling, a first-order approximation to the behavior shown in Fig. 5 is possible. We have found that for $t < 600 \mu\text{s} \ll \tau$, the fluorescence level changes linearly in response to recoiling. This allows us to determine the fluorescence rate at $t = 0$ independently from a model of the recoiling dynamics. We analyze the fluorescence curves such as in Fig. 5 by using varying bin size. For each bin-size, we take the ratio of counts in the initial bin (S_0) divided by the counts per bin at equilibrium (S_∞). From the linear change of the fluorescence level, we extrapolate to the level that would have been obtained for zero bin-size. The method is illustrated in Fig. 7. It provides us with a precise value of the fluorescence level at the beginning of recoiling. The change of fluorescence with respect to the equilibrium level obtained in this way is indicated in Fig. 5 by an arrow.

In order to extract the ion's temperature from the fluorescence measurement at $t = 0$, we use the method discussed in Sect. 4, based on the spectrum of the ion. In a first step, we measure the fluorescence spectrum of the Doppler-cooled ion, yielding the equilibrium fluorescence level $S_\infty(\delta)$ and, from S_{cooled} in Eq. (8) in the Appendix, the power-broadened linewidth γ . An example is shown in Fig. 8. It serves as a reference for the determination of the heated spectrum, indicating the asymptotic fluorescence level approached in the recoiling process.

In a second step, we determine the change of fluorescence level from hot to cold ion, S_0 to S_∞ , from recoiling curves like that in Fig. 5 as described above. The ratio R of the two values can be compared directly to the corresponding

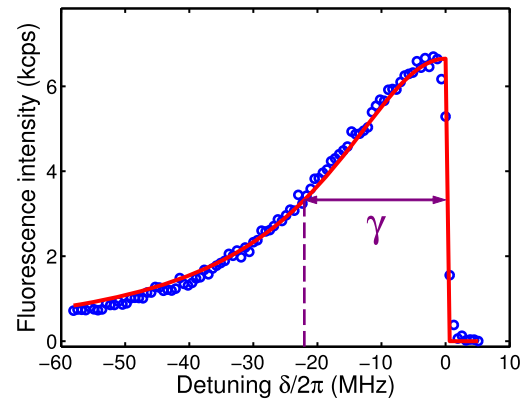


Fig. 8 Fluorescence spectrum of the Doppler-cooled ion, obtained under steady-state conditions. It corresponds to S_{cooled} in Fig. 6 and provides the reference level $S_\infty(\delta)$ for measuring the fluorescence of the heated ion. The measured linewidth is $\gamma = 2\pi \times 21.9$ MHz, corresponding to a saturation parameter $s = (\gamma/\gamma_0)^2 - 1 = 2.9$

theoretical expression, obtained from the spectra given by Eqs. (8) and (5).

$$R(\delta, \gamma, \sigma, \Delta_0) = \frac{S_{\text{heated}}(\delta, \gamma, \sigma, \Delta_0)}{S_{\text{cooled}}(\delta, \gamma)} - 1 \stackrel{!}{=} S_0/S_\infty - 1. \quad (6)$$

With γ already determined from the cooled spectrum, fitting the theoretical expression (6) to the relative change of the fluorescence level allows us to determine the values of thermal broadening σ and oscillatory motion Δ_0 . As the radiation pressure of the laser depends on detuning, so does the amplitude z_0 of oscillatory motion after the laser is switched off. We accommodate this by using a detuning-dependent expression for Δ_0 .

$$\Delta_0(\delta) = \Delta_{00} \frac{\gamma^2 - \gamma_0^2}{\gamma^2 + \delta^2}, \quad (7)$$

where γ_0 is the natural linewidth of the transition and Δ_{00} is the maximum Doppler shift for resonant radiation pressure.

The result of the fit for four different detunings of the laser is shown in Fig. 9. Each data point falls on the theoretical curve corresponding to the value of γ used for this measurement, as indicated by different colors. It is not possible to fit the data in Fig. 9 with a model neglecting the oscillatory motion of the ion (cf. the dashed trace in the figure). These results confirm that the expression (5) accurately describes the ion's spectrum at the end of the heating phase.

Having obtained the value of Δ_{00} and σ from the fit, the temperature of the ion at the end of the heating period is determined using Eq. (4). As long as the laser power is kept constant, γ is identical for all measurements. Therefore, σ and hence the temperature is the only unknown parameter in expression (6). It can be determined by working at a fixed detuning which we have chosen as $\delta = -2\pi \times 11$ MHz.

In this way, we have determined the temperature of the ion for different heating times τ . The results are shown in

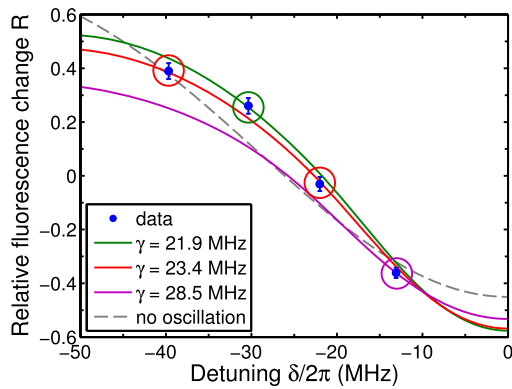


Fig. 9 Measured values for the relative fluorescence change $R = (S_0/S_\infty - 1)$ after 500 ms of heating. Three different theoretical fit curves are shown to accommodate the independently determined homogeneous linewidths which are slightly different for each measurement. The oscillatory motion and inhomogeneous linewidth of the ion are obtained from a fit using all data points as $\Delta_{00} = 2\pi \times 66.4$ MHz and $\sigma = 2\pi \times 24.5$ MHz. This corresponds to a temperature of $T = 457$ mK. The *dashed line* shows the inadequate fit obtained when the oscillatory motion of the ion is neglected

Fig. 10. The increase of temperature with heating time is roughly linear, the slope defining the heating rate of the ion in our trap. We obtain a value of $dT/d\tau = (2.0 \pm 0.1)$ mK/ms. Note that for $\tau \rightarrow 0$, the temperature approaches zero, as it should be starting from an ion cooled to the Doppler temperature at a level of 1 mK. The effect of neglecting the oscillatory motion of the ion is also demonstrated in Fig. 10. The green circles indicate the temperatures that would have been obtained in this case. The apparent heating rate would have been 15 % smaller, but the biggest problem is the resulting offset of 570 mK at $\tau = 0$, three orders of magnitude larger than the Doppler temperature of the ion. This is clearly impossible, as at $\tau \approx 0$, no thermal heating could have occurred, and hence no measurable increase in temperature. Observation of substantial temperature offsets in other heating-rate experiments shows that radiation-pressure induced oscillations of the ion are a phenomenon that must be taken into account to arrive at correct values for the ion temperature.

From the observed heating rate, a spectral density of electric field fluctuations of $S_E(\omega) = 3 \times 10^{-10}$ V²/m² Hz is obtained at an ion-electrode distance of 166 μ m. This compares well with measurements of heating in other traps of the same size [25, 26]. The result is remarkable, given the limited surface quality of the copper electrodes, which is a potential source of increased heating, and the presence of stray fields found in micromotion compensation.

6 Conclusions

In conclusion, we have developed and thoroughly characterized a novel microscopic ion trap based on convention-

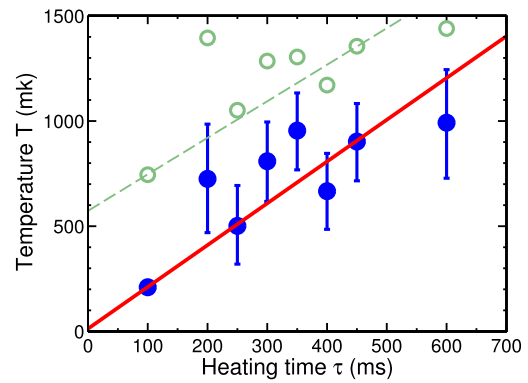


Fig. 10 Measured temperature of the ion as a function of heating time. The heating rate is determined from the slope of a linear fit (*solid line*) to be $dT/d\tau = (2.0 \pm 0.1)$ mK/ms. The temperature measurement is most precise for the data point at $\tau = 100$ ms, which has error bars smaller than the size of the marker. The open green circles indicate the temperature values that would have been obtained from a model neglecting oscillatory motion of the ion. The corresponding linear fit, shown as a *dashed line*, wrongly results in a slightly lower heating rate and a large temperature offset of 570 mK

ally machined components. It has been constructed to enable cavity-QED experiments in the strong coupling regime at a cavity length of 500 μ m which requires minimizing the overlap between the trapping fields and the cavity mirrors. We have investigated the long term behavior of micromotion in the trap and found that the most significant contributions to fluctuating stray fields are likely to originate in changing patch potentials during the loading process.

In order to measure the heating rate of ions in our trap, we employed the Doppler-recooling method, combined with a novel analysis of the ion's spectrum during the measurement. We have found an analytical expression for the spectrum which includes homogeneous and inhomogeneous broadening, and for the first time, takes into account harmonic oscillation of the ion induced by radiation pressure. The resulting heating rate of $dT/d\tau = (2.0 \pm 0.1)$ mK/ms is comparable to that of other traps with a similar size in spite of the surface roughness and the unusual electrode material. It is worth noting that for experiments with ions in cavities, it is sufficient to reach the Lamb–Dicke regime of ion localization, which extends to a thermal excitation of a few hundred vibrational quanta. At the measured heating rate, the system will remain in the Lamb–Dicke regime for milliseconds, which is long compared to cavity-enhanced ion-photon coupling rate on the order of MHz. The observed heating rate is therefore no constraint for achieving controlled ion-cavity interaction in the trap.

Acknowledgement We gratefully acknowledge support from the European Commission (Marie Curie Excellence Grant MEXT-CT-2005-025703, SCALA network Contract 015714) and the EPSRC (EP/D061296/1).

Appendix: Line shape of an oscillating hot ion

In this Appendix, we consider the fluorescence line shape of a trapped ion exposed to intermittent excitation. The treatment of homogeneous broadening and thermal Doppler broadening is similar to the one in Ref. [24] (note that we use angular frequencies instead of scaled parameters). The most important distinguishing feature of our model is that it includes the oscillatory motion of the ion in the harmonic trapping potential resulting from the interruption of radiation pressure. For the first time, we derive an analytic expression for the spectrum of the ion under these conditions. It allows us to determine the temperature of the ion from the spectrum, without relying on the details of the recoiling dynamics used in Ref. [24], which would be difficult to model in the presence of radiation pressure.

We start by considering the case of homogeneous broadening, applicable to a cold ion at rest in the trapping potential. The normalized spectrum, which is proportional to the fluorescence intensity measured in the experiment is given by a Lorentzian

$$S_{\text{cooled}}(\delta, \gamma) = \frac{\gamma}{\pi} \frac{1}{\gamma^2 + \delta^2}, \tag{8}$$

where δ is the detuning from resonance and γ is the half width at half maximum of the transition due to homogeneous broadening. When the ion is not at rest but undergoing oscillatory motion in the trapping potential, a periodically changing Doppler shift occurs, given by

$$\Delta(t) = \Delta_0 \cos \omega_z t, \tag{9}$$

where oscillation along the trap-axis (z -direction) with frequency ω_z is assumed and the amplitude Δ_0 is given by Eq. (2).

The periodic Doppler shift leads to a modified spectrum

$$S_D(\delta, \gamma, \Delta_0) = \frac{1}{\pi} \text{Re} \left[\frac{1}{\sqrt{\Delta_0^2 - (\delta + i\gamma)^2}} \right]. \tag{10}$$

For an ion undergoing thermal motion, spectrum (10) must be averaged over a distribution of Doppler shift amplitudes Δ_0 . It is convenient to express the Doppler shift through the oscillatory energy $\epsilon = m\omega_z^2 z_0^2/2$ of the ion and the recoil energy $E_r = \hbar^2/2m\lambda^2$ [24]:

$$\hbar\Delta_0 = \frac{\hbar z_0 \omega_z}{\lambda} = \sqrt{4\epsilon E_r}. \tag{11}$$

The probability distribution for oscillation energy ϵ of the ion is given by

$$P(\epsilon, \bar{\epsilon}) = \frac{1}{\bar{\epsilon}} \exp\left(\frac{-\epsilon}{\bar{\epsilon}}\right). \tag{12}$$

The thermally broadened spectrum is then obtained as

$$S_{\text{therm}}(\delta, \gamma, \sigma) = \int_0^\infty P(\epsilon, \bar{\epsilon}) S_D(\delta, \gamma, \sqrt{4\epsilon E_r/\hbar}) d\epsilon, \tag{13}$$

with $\hbar\sigma = \sqrt{2E_r\bar{\epsilon}}$. The integral can be evaluated and expressed in analytical form

$$S_{\text{therm}}(\delta, \gamma, \sigma) = \frac{1}{\sqrt{2\pi}\sigma} \text{Re} \left[w\left(\frac{|\delta| + i\gamma}{\sqrt{2}\sigma}\right) \right]. \tag{14}$$

The function $w(z)$ is the Faddeeva function or complex error function, given by

$$w(z) = \exp(-z^2)(1 - \text{erf}(-iz)) \tag{15}$$

and can be readily computed [27]. Expression (14) is identical to a Voigt profile with inhomogeneous linewidth σ .

In the experimental configuration described in this paper, switching off the cooling laser results in the ion undergoing an oscillation with a fixed amplitude z_0 , even before it starts heating up. This can be accommodated by using a modified distribution function, spread around an oscillation at fixed energy $\epsilon_0 = (\hbar\Delta_0)^2/4E_r$.

$$P_{\text{osc}}(\epsilon, \epsilon_0) = \frac{1}{\bar{\epsilon}[2 - \exp(-\epsilon_0/\bar{\epsilon})]} \exp\left(-\frac{|\epsilon - \epsilon_0|}{\bar{\epsilon}}\right). \tag{16}$$

The spectrum of a hot ion including homogeneous broadening, harmonic oscillation and thermal effects is therefore given by

$$S_{\text{heated}}(\delta, \gamma, \sigma, \Delta_0) = \int_0^\infty P_{\text{osc}}(\epsilon, \epsilon_0) S_D(\delta, \gamma, \sqrt{4\epsilon E_r/\hbar}) d\epsilon. \tag{17}$$

The integral in (17) can be solved analytically, again using the Faddeeva function, leading to the expression given in Eq. (5) in Sect. 4.

$$S_{\text{heated}}(\delta, \gamma, \sigma, \Delta_0) = \text{Re} \left[\frac{w(\sqrt{z-d}) - iw(\sqrt{d-z^*}) + ie^{-d}w(\sqrt{-z^*})}{\sqrt{2\pi}\sigma(2 - e^{-d})} \right]$$

where

$$z = \frac{(|\delta| + i\gamma)^2}{2\sigma^2}, \quad d = \frac{\Delta_0^2}{2\sigma^2}$$

and $w(z)$ is defined in Eq. (15). It is easy to see that for negligible oscillatory motion of the ion ($\Delta_0 \rightarrow 0$), the above expression reduces to (14), i.e., a Voigt-profile.

Expression (5) describes the most general fluorescence spectrum of a trapped ion. To our knowledge, it has not been derived in analytic form before. In the experiment, the homogeneous linewidth γ is determined by power broadening of the natural linewidth, σ is related to the temperature of the ion and Δ_0 is either due to secular motion in the trap or due to micromotion. Oscillation along the axis of the linear trap is initiated as a result of the sudden switch-off of the cooling laser at the beginning of the heating period. Radiation pressure of the cooling laser displaces the equilibrium position of the ion by an amount z_0 in the axial potential well.

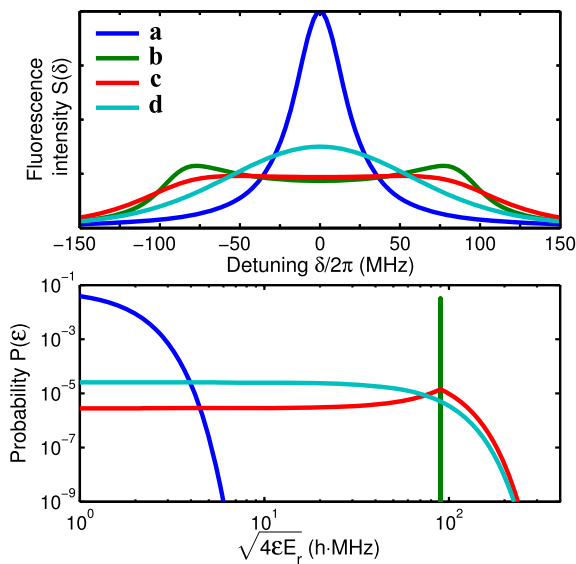


Fig. 11 Fluorescence spectra $S(\delta)$ calculated from Eq. (5) for different sets of parameters. (a) $(\gamma, \sigma, \Delta_0) = 2\pi \times (20, 1, 0)$ MHz, corresponding to homogeneous broadening (Lorentzian profile); (b) $(\gamma, \sigma, \Delta_0) = 2\pi \times (20, 1, 90)$ MHz, corresponding to a cold oscillating ion; (c) $(\gamma, \sigma, \Delta_0) = 2\pi \times (20, 50, 90)$ MHz, corresponding to a hot oscillating ion; (d) $(\gamma, \sigma, \Delta_0) = 2\pi \times (20, 50, 0)$ MHz, corresponding to a hot ion with no oscillation (Voigt profile). The graph below shows the corresponding probability distributions $P(\epsilon)$, plotted as a function of the scaled energy $\sqrt{4\epsilon E_r}$

Removal of radiation pressure therefore launches oscillatory motion with amplitude z_0 .

Figure 11 shows fluorescence spectra calculated from Eq. (5) for different parameters. In the figure below, the corresponding distribution of oscillation energies, which appears explicitly in Eq. (17), is plotted. While an oscillating ion is characterized by a delta-function (case (b), green line), adding thermal motion leads to a broader distribution. In case (c), red line, there is still a peak at the original oscillation energy. It is, however, approaching the pure thermal distribution of case (d).

References

1. F. Diedrich, H. Walther, Phys. Rev. Lett. **58**, 203 (1987)
2. T. Rosenband, D.B. Hume, P.O. Schmidt, C.W. Chou, A. Brusch, L. Lorini, W.H. Oskay, R.E. Drullinger, T.M. Fortier, J.E. Stalnaker, S.A. Diddams, W.C. Swann, N.R. Newbury, W.M. Itano, D.J. Wineland, J.C. Bergquist, Science **319**, 1808 (2008)
3. T. Schneider, E. Peik, C. Tamm, Phys. Rev. Lett. **94**, 230801 (2005)
4. F. Schmidt-Kaler, H. Häffner, M. Riebe, S. Gulde, G.P.T. Lancaster, T. Deuschle, C. Becher, C.F. Roos, J. Eschner, R. Blatt, Nature **422**, 408 (2003)
5. D. Leibfried, B. DeMarco, V. Meyer, D. Lucas, M. Barrett, J. Britton, W.M. Itano, B. Jelenkovic, C. Langer, T. Rosenband, D.J. Wineland, Nature **422**, 412 (2003)
6. T. Monz, P. Schindler, J. Barreiro, M. Chwalla, D. Nigg, W. Coish, M. Harlander, W. Hänsel, M. Hennrich, R. Blatt, Phys. Rev. Lett. **106**, 130506 (2011)
7. G.R. Guthöhrlein, M. Keller, K. Hayasaka, W. Lange, H. Walther, Nature **414**, 49 (2001)
8. M. Keller, B. Lange, K. Hayasaka, W. Lange, H. Walther, Nature **431**, 1075 (2004)
9. H.G. Barros, A. Stute, T.E. Northup, C. Russo, P.O. Schmidt, R. Blatt, New J. Phys. **11**, 103004 (2009)
10. J.I. Cirac, P. Zoller, H.J. Kimble, H. Mabuchi, Phys. Rev. Lett. **78**, 3221 (1997)
11. D. Stick, W.K. Hensinger, S. Olmschenk, M.J. Madsen, K. Schwab, C. Monroe, Nat. Phys. **2**, 36 (2006)
12. J. Chiaverini, R.B. Blakestad, J. Britton, J.D. Jost, C. Langer, D. Leibfried, R. Ozeri, D.J. Wineland, Quantum Inf. Comput. **5**, 419 (2005)
13. J. Britton, D. Leibfried, J.A. Beall, R.B. Blakestad, J.H. Wesenberg, D.J. Wineland, Appl. Phys. Lett. **95**, 173102 (2009)
14. M. Keller, B. Lange, K. Hayasaka, W. Lange, H. Walther, Appl. Phys. B **76**, 125 (2003)
15. M.A. Rowe, A. Ben-Kish, B. Demarco, D. Leibfried, V. Meyer, J. Beall, J. Britton, J. Hughes, W.M. Itano, B. Jelenkovic, C. Langer, T. Rosenband, D.J. Wineland, Quantum Inf. Comput. **2**, 257 (2002)
16. D.M. Lucas, A. Ramos, J.P. Home, M.J. McDonnell, S. Nakayama, J.P. Stacey, S.C. Webster, D.N. Stacey, A.M. Steane, Phys. Rev. A **69**, 012711 (2004)
17. D.J. Berkeland, J.D. Miller, J.C. Bergquist, W.M. Itano, D.J. Wineland, J. Appl. Phys. **83**, 5025 (1998)
18. N. Seymour-Smith, P. Blythe, M. Keller, W. Lange, Rev. Sci. Instrum. **81**, 075109 (2010)
19. M. Harlander, M. Brownnutt, W. Hänsel, R. Blatt, New J. Phys. **12**, 093035 (2010)
20. Q.A. Turchette, D. Kielpinski, B.E. King, D. Leibfried, D.M. Meekhof, C.J. Myatt, M.A. Rowe, C.A. Sackett, C.S. Wood, W.M. Itano, C. Monroe, D.J. Wineland, Phys. Rev. A **61**, 063418 (2000)
21. L. Deslauriers, S. Olmschenk, D. Stick, W.K. Hensinger, J. Sterk, C. Monroe, Phys. Rev. Lett. **97**, 103007 (2006)
22. U.G. Poschinger, G. Huber, F. Ziesel, M. Deiss, M. Hettrich, S.A. Schulz, K. Singer, G. Poulsen, M. Drewsen, R.J. Hendricks, F. Schmidt-Kaler, J. Phys. B, At. Mol. Opt. Phys. **42**, 154013 (2009)
23. R.J. Epstein, S. Seidelin, D. Leibfried, J.H. Wesenberg, J.J. Bollinger, J.M. Amini, R.B. Blakestad, J. Britton, J.P. Home, W.M. Itano, J.D. Jost, E. Knill, C. Langer, R. Ozeri, N. Shiga, D.J. Wineland, Phys. Rev. A **76**, 033411 (2007)
24. J.H. Wesenberg, R.J. Epstein, D. Leibfried, R.B. Blakestad, J. Britton, J.P. Home, W.M. Itano, J.D. Jost, E. Knill, C. Langer, R. Ozeri, S. Seidelin, D.J. Wineland, Phys. Rev. A **76**, 053416 (2007)
25. J.M. Amini, J. Britton, D. Leibfried, D.J. Wineland, in *Atom Chips*, ed. by J. Reichel, V. Vuletic (Wiley-VCH, Weinheim, 2011), Chap. 13, pp. 395–416
26. N. Daniilidis, S. Narayanan, S.A. Möller, R. Clark, T.E. Lee, P.J. Leek, A. Wallraff, S. Schulz, F. Schmidt-Kaler, H. Häffner, New J. Phys. **13**, 013032 (2011)
27. J.A.C. Weideman, SIAM J. Numer. Anal. **31**, 1497 (1994)